Materials Science & Engineering A 587 (2013) 304–312

Contents lists available at ScienceDirect

Materials Science & Engineering A

journal homepage: www.elsevier.com/locate/msea

Stress induced pop-in and pop-out nanoindentation events in CuAlBe shape memory alloys

C. Caër*, E. Patoor, S. Berbenni, J.-S. Lecomte

Laboratoire d'Étude des Microstructures et de Mécanique des Matériaux (LEM3), UMR CNRS 7239, Université de Lorraine, Arts et Métiers ParisTech, 57070 Metz, France

ARTICLE INFO

Article history:
Received 9 July 2013
Accepted 24 August 2013
Available online 6 September 2013

Keywords:
Nanoindentation
Martensitic phase transformation
SMA
Pop-in
Pop-out
Indentation Patel–Cohen factor

ABSTRACT

Constitutive models developed to predict Shape Memory Alloys (SMA) behavior are often based on a simplified phenomenological description of martensite variant activation under thermomechanical loading at the micro scale. This study aims at modeling and characterizing by nanoindentation the discrete variant activation events at the nanoscale. A new criterion is proposed to describe martensite variant activation beneath the indenter. Evidence of discrete martensitic transformation is observed during nanoindentation by the successive occurrences of pop-in and pop-out load events on the force versus displacement curve during respectively loading and unloading. Thus, the spatial-temporal discontinuity of phase transformation activation and propagation is highlighted at the nanoscale with the introduction of an indentation Patel–Cohen factor for both forward austenite–martensite and reverse phase transformations. Dislocation emission in pure nickel is first studied to validate both the nanoindentation testing procedure using a Berkovich indenter and the calculations of indentation Schmid factors to describe excursion bursts corresponding to dislocation activation and propagation. Good agreement is found between nanoindentation tests performed on a superelastic CuAlBe SMA and theoretical crystallographic dependence of pop-in and pop-out loads predicted by the new introduced indentation Patel and Cohen factor.

© 2013 Elsevier B.V. All rights reserved.

1. Introduction

Shape Memory Alloys (SMA) undergo a reversible thermoelastic martensitic phase transformation which is due to a displacive, diffusionless, first order phase transition. SMA can exhibit a specific behavior called superelasticity which is associated with stress induced transformation. When the material is loaded at some specific constant temperature the austenitic parent phase transforms from austenite to martensite and large amounts of inelastic strains are developed. Upon unloading back to the zero stress state the material undergoes a reverse phase transformation from martensite back to austenite where inelastic deformations are recovered [1]. Constitutive micromechanical models developed to predict Shape Memory Alloys (SMA) behaviors are often based on a simplified phenomenological description of martensite variant activation under thermomechanical loading at the microscale [2,3].

Instrumented indentation has been widely developed in recent years to study material's mechanical properties such as hardness, Young's modulus [4] or even local strain hardening [5] at small scales. This technique is very useful to characterize discrete mechanisms at the nanoscale such as oxide breaking [6,7], microcracking [8], homogeneous dislocation nucleation [9–13], and stress-induced phase transformation [14,15]. Incipient plasticity has been characterized on a wide range of materials by the occurrence of an excursion event, called pop-in, on the loading part of the nanoindentation curve. Woirgard et al. [16] observed a displacement burst during the unloa;ding of the nanoindentation curve on a silicon single crystal. This excursion event, denoted pop-out, was explained as phase transformation as neither slip lines associated with incipient plasticity nor microcracks were observed beneath the indenter.

Applied to superelastic SMA nanoindentation is an experimental way of investigating their thermomechanical properties and their evolution with heat treatments [17], but also to study the martensitic transformation at the nanoscale. Martensitic phase transformation has been mostly studied using nanoindentation in NiTi SMA [18–20] and a few studies have been led on superelastic CuAlNi [21,22]. This completely reversible phase transition is characterized on the nanoindentation curve (load versus displacement) by the occurrence of displacement bursts during both loading and unloading and by zero residual displacement after complete unloading. Frick et al. [23] have observed discrete phase transformation events on shape memory and superelastic NiTi

* Correspondence to: LEM3, Université de Lorraine, Arts et Métiers ParisTech, UMR CNRS 7230, 4, rue Augustin Fresnel, 57070 Metz, France. Tel.: +33 387 37 54 30.
E-mail address: celia.caer@ensam.eu (C. Caër).

0921-5093/$ - see front matter © 2013 Elsevier B.V. All rights reserved.
http://dx.doi.org/10.1016/j.msea.2013.08.052

alloys using nanoindentation. These authors showed that the detection of such mechanisms by nanoindentation is very difficult due to the shortness of excursion events and the small loads at which these events occur. This is the reason why the relevance of the nanoindentation study is first validated on the pop-in detection in pure nickel (Ni). NiTi alloys are the most studied Shape Memory Alloys because of their industrial applications. However NiTi alloys are not the best candidates to study martensitic transformation at small scale because in these alloys phase transition is usually coupled with plasticity [24] and it is then difficult to set apart the effect of one inelastic mechanism from the other. The present study investigates a CuAlBe SMA. This copper-based alloy was chosen for its large grain size and for the presence of beryllium in the matrix. CuAlBe alloys present a large grain size compared to NiTi alloys which gives the opportunity to perform extensive nanoindentation tests on one single crystal. The addition of beryllium in interstitial solid solution hardens the matrix and increases the plastic yield stress of the parent phase, favouring phase transition activation and limiting plasticity nucleation [25]. One of the objectives of this paper is to show evidence of discrete phase transformation events at the nanoscale in a superelastic CuAlBe shape memory alloy identified as pop-in and pop-out events and to investigate the orientation dependence of martensitic variant activation at this scale.

Whereas martensitic transformation has been experimentally investigated using nanoindentation, few efforts have been made to develop activation criteria in order to understand phase transformation under such mechanical tests. Pfetzing-Micklich et al. [26] studied the influence of crystal orientation on martensitic transformation beneath the indenter in NiTi SMA using molecular dynamics simulations. They found that the hardness curves can be correlated with the martensite volume occupied beneath the indenter which is dependent on crystal orientation, however they did not study pop-in and pop-out events at small loads. The present study investigates a new criterion called indentation Patel–Cohen factor, based on a continuum thermo-micromechanics approach and Hertzian elastic contact theory to predict the activation of the first martensite variant beneath the indenter as a function of crystal orientation. This Patel–Cohen factor relies on the computation of the driving forces associated to variants activation during the first pop-in load. Conversely, it is also shown that the indentation Patel–Cohen factor can also be applied to the last pop-out load corresponding to the reverse phase transformation from martensite back to (elastic) austenite. The validation of the stress tensor calculation is first performed on the indentation Schmid factors in comparison with the recent work of Li et al. [27]. Then, the indentation Patel–Cohen factors are discussed in the light of the present experimental nanoindentation curves and results performed on CuAlBe SMA. To the knowledge of the present authors such a criterion has not been described in the literature.

This paper is organized as follows. In Section 2, Ni and CuAlBe specimens used in this study are presented. Both surface preparation and nanoindentation experimental procedure are detailed for each material. In Section 3, the main equations using the elastic contact with axisymmetric indenter are used to calculate the indentation Schmid factor for crystal plasticity and the new indentation Patel–Cohen factor for direct and reverse phase transformations. In Section 4, the nanoindentation results are presented for several crystallographic orientations in Ni and CuAlBe specimen. The calculations of indentation Schmid factor are applied to three orientations in the case of Ni, in order to validate both stress field analysis and experimental procedure. Finally, nanoindentation results for three different crystallographic orientations of the CuAlBe SMA specimen are presented, discussed, and compared to the calculated indentation Patel–Cohen factors. Section 5 concludes and sketches some perspectives to this work.

2. Experimental procedure

2.1. Materials

A polycrystalline plate of CuAlBe shape memory alloy (Cu–12 wt% Al–0.5 wt%Be) was used in the present investigation. The specimen exhibits the following transformation temperatures: Ms = 269 K, Mf = 279 K, As = 243 K and Af = 265 K (respectively martensite start and finish and austenite start and finish temperature). The sample specimen is initially in the austenitic state (f.c.c. crystallographic structure) at room temperature and shows a superelastic behavior. The average grain size of the specimen is about one millimeter which is large enough according to the indenter size to consider the indented grain as a single crystal. In addition a polycrystalline specimen of commercially pure Ni (> 99.99%) (FCC crystallographic structure) was also used in this study to validate the experimental procedure. The grain size of the Ni specimen is around 140 μm which is also large enough to consider nanoindentation on a crystal.

2.2. Surface preparation

Both specimens were first mechanically polished with decreasing SiC paper and particulate diamond paste. The final mechanical polish was performed with a 1 μm diamond paste. Finally they were electropolished in a solution of (C_2H_5OH (25 mL) + H_3PO_4 (25 mL) + H_2O) with a DC voltage of 20 V for CuAlBe and in a solution of (H_2SO_4 (20 mL) + CH_3OH (80 mL)) with a DC voltage of 35 V for the Ni specimen. Prior to nanoindentation tests EBSD mappings were performed in order to determine the crystallographic orientation of the grains.

2.3. Nanoindentation

Nanoindentation measurements were conducted using a commercial CSM Instruments “NHT2” nanoindentation head. This device is fitted with a reference ring taking the depth reference directly on the specimen surface, to avoid long waiting for thermal drift stabilization. Tests were performed using two Berkovich tips. The radius of curvature of the indenter tips were estimated on the basis of AFM measurements to be approximately 300 ± 33 nm for the tip used on Ni and 1 ± 0.3 μm for the indenter used on the CuAlBe specimen.

Nanoindentation measurements were performed on Ni on three grains A_1, A_2, A_3 with a crystal orientation respectively close to [001], [101], [111], and on three grains B_1, B_2 and B_3 of CuAlBe with respective orientation close to [001], [001], [111]. The indented grain orientations are close enough to ideal orientations to approximate their properties with ideal orientations properties.

Distinct nanoindentation procedures were set up for CuAlBe and Ni. For both materials nanoindentation tests were performed under applied load P with a constant rate of $\dot{P}/P = 0.125\ s^{-1}$ for Ni and $\dot{P}/P = 0.01\ s^{-1}$ for CuAlBe. In the case of the superelastic SMA, it is possible to perform several indentations at the same location considering each test independently from others due to the superelastic behavior of the material and the absence of residual strain (no plastic deformation) after a nanoindentation measurement. Thus, for the SMA the loading test sequence was made up of four loading–unloading cycles up to 100 μN for grains B_1 and B_2 and 500 μN for grain B_3. The minimum load P between two consecutive cycles was set to 2 μN to keep contact between the Berkovich indenter tip and the specimen surface. The objective of the first cycle is to break the oxide layer, and the data from the three following cycles were used for the study. These cycles of loading–unloading at the same position are not relevant for tests on Ni, were irreversible plasticity is produced. Nanoindentation tests on this material were set up of a unique cycle of loading–unloading up to a maximum load of 800 μN.

Indentations were operated at sufficiently large distance from the grain boundary to avoid any interaction between the stress field generated by the indentation and the elastic incompatibility stresses associated to the presence of a grain boundary. For tests performed on Ni a distance of 30 μm was respected between each indentation to avoid any interaction between the incompatibility stresses and stresses generated within the crystal by the current indent load.

3. Indentation factor

3.1. Effective modulus

Using elastic Hertzian theory of a sphere in contact with a semi-infinite half space, the equation used to illustrate the idealized elastic contact is

$$P=\frac{4}{3}E_r\sqrt{R\,h^3} \tag{1}$$

where P is the applied load (see Section 2.3), h the penetration depth, R the radius of the indenter tip and E_r the reduced modulus. Here, material's elastic anisotropy is considered in the reduced modulus. The anisotropic elastic reduced modulus is related to the elastic isotropic modulus E_i and Poisson ratio ν_i of the Berkovich indenter (for a diamond tip: E_i=1141 GPa, ν_i=0.07) and to the effective indentation modulus of the specimen as follows [28]:

$$E_r=\left(\frac{1-\nu_i^2}{E_i}+\frac{1}{E_{eff}^{(hkl)}}\right)^{-1} \tag{2}$$

The effective indentation modulus is computed from the expression given by Vlassak and Nix [28,29]:

$$E_{eff}^{(hkl)}=\beta_{(hkl)}\frac{E_s}{1-\nu_s} \tag{3}$$

where E_s and ν_s are respectively the isotropic Young's modulus and Poisson ratio of the specimen. Values taken for the isotropic E_s and ν_s are issued from Simmons et al. [30] for Ni and from Sánchez-Arévalo et al. [31] for CuAlBe and Kaouache [25] and presented in Table 1. From [29], $\beta_{(hkl)}$ is defined as

$$\beta_{(hkl)}=a+c\,(A-A_0)^B \tag{4}$$

where A is the anisotropy factor of the sample depending on the material elastic constants: $A=2\,c_{44}/(c_{11}-c_{12})$. c_{11}, c_{12} and c_{44} are the three independent elastic moduli in the cubic symmetry. The other constants a, c, A_0 and B are related to the crystal orientation, determined from Vlassak and Nix's tables [29]. In these tables, the choice of these constants require the calculation of the Poisson's ratio in the [100] direction: $\nu_{<100>}=-\frac{s_{12}}{s_{11}}=c_{12}/(c_{12}+c_{11})$, where s_{11}, s_{12} are two of the three elastic compliances. The elastic constants values presented in Table 1 for both Ni and CuAlBe are respectively issued from Li et al. [27] and Rios-Jara et al. [32]. The calculated anisotropy factor A and Poisson's ratio $\nu_{<100>}$ are also reported in Table 1 for the two studied materials. The values obtained for $\nu_{<100>}$ are 0.38 for Ni (rounded up to 0.4) and 0.47 for CuAlBe (rounded up to 0.47).

Vlassak and Nix's table [29] is set up for anisotropy factors contained between 0.6 and 8. Thus, the use of these tables is relevant for Ni but not obviously for CuAlBe which presents an anisotropy factor superior to 8. Eq. (4) was yet used to calculate the CuAlBe effective modulus for the ideal [001] and [111] orientations, considering $\nu_{<100>}=0.45$ and $A=13$. Results are presented in Table 2. In order to validate these results, another method reported by Vlassak and Nix [28] is used. It consists in extrapolating abaqus representing normalized indentation modulus E_N versus anisotropy factor and Poisson's ratio in the [100] direction up to $A=13$. The corresponding E_N is then reported and the effective modulus is obtained according to: $E_{eff}=E_N E_s/(1-\nu_s^2)$. Good agreement was found between the values of E_{eff} calculated using the two methods. Resulting effective modulus and reduced modulus for the [001], [101] and [111] of Ni and [001] and [111] of CuAlBe are presented in Table 2.

3.2. Indentation stress field

The stress field due to an axisymmetric indenter under the hypothesis of linear isotropic elasticity was determined from integrals adapted from equations (3.19) of Johnson [33]. This stress field is not homogeneous beneath the tip, unlike pure uniaxial compression tests. The integrals were numerically computed using a Gauss–Legendre integration procedure [34]. The ratio of the stress components at some arbitrary position (x,y,z) to the maximum contact pressure p_0 for a circular contact of radius a are computed according to the following integration:

$$\frac{\sigma_{ij}(x/a,y/a,z/a)}{p_0}=\int_0^a\int_0^{2\pi}\tilde{p}(x',y')\tilde{\sigma}_{ij}(x/a-x',y/a-y',z/a)\mathrm{rd}\theta\mathrm{d}r \tag{5}$$

where $x'=r\cos\theta$, $y'=r\sin\theta$, and the stress components $\tilde{\sigma}_{ij}$ are due to a point force contact (the components $\tilde{\sigma}_{ij}$ are reported in the Appendix). The surface pressure distribution $\tilde{p}$ for a circular contact is given by

$$\tilde{p}(x',y')=\sqrt{1-\frac{x'^2+y'^2}{a^2}} \tag{6}$$

The maximum contact pressure is defined as follows:

$$p_0=\left(\frac{6PE_r^2}{\pi^3R^2}\right)^{1/3} \tag{7}$$

and describes the elastic regime until the first inelastic event occurs during indentation loading. At the first loading stages, the stress field under the indenter first induces elastic strain, and with the increasing of the applied load, other types of deformation such as plastic strain or transformation strain are activated at a given threshold stress. These threshold stresses are experimentally obtained from pop-in or pop-out loads.

3.3. Indentation Schmid factor for crystal plasticity

When a nanoindentation loading is applied to a single crystal showing an elasto-plastic behavior, the first material response is elastic up to a threshold stress at which crystal plasticity occurs under single slip. For the activation of a single slip system (v), the

Table 1
Isotropic Young's modulus, Poisson's ratio, elastic constants and calculated anisotropy factor and Poisson's ratio in the [100] direction for both Nil and CuAlBe.

	E_s (GPa)	ν_s	c_{11} (GPa)	c_{12} (GPa)	c_{44} (GPa)	A	$\nu_{<100>}$
Ni	192.5	0.33	244	158	102	2.4	0.38
CuAlBe	110	0.3	138	124	93	13	0.47

Table 2
Effective nanoindentation and reduced moduli for Ni ideal orientation and austenitic CuAlBe ideal orientations.

Ideal orientation	$[001]_{Ni}$	$[101]_{Ni}$	$[111]_{Ni}$	$[001]_{CuAlBe}$	$[111]_{CuAlBe}$
E_{eff} (GPa)	202	219	224	99	133
E_r (GPa)	172	184	187	91	119

induced plastic strain in the volume crystal reads:

$$\varepsilon_{ij}^{P} = \gamma^{(v)} R_{ij}^{(v)} \tag{8}$$

where $\gamma^{(v)}$ is the slip magnitude and $R_{ij}^{(v)}$ is the Schmid tensor, expressed as follows:

$$R_{ij}^{(v)} = \frac{1}{2}(n_i^{(v)} s_j^{(v)} + n_j^{(v)} s_i^{(v)}) \tag{9}$$

where $n_i^{(v)}$ and $s_i^{(v)}$ are respectively the slip normal and the slip direction of the slip system (v). The resolved shear stress $\tau_R^{(v)}$ is defined as

$$\tau_R^{(v)}(x,y,z) = R_{ij}^{(v)} \sigma_{ij}(x,y,z) \tag{10}$$

It consequently depends on the position (x, y, z) beneath the indenter and on the considered slip system (v) running from 1 to the total number of possible slip systems (12 slip systems are considered in f.c.c. crystals).

To determine the influence of crystallographic orientation on the initial yield point under Hertzian contact, Li et al. [27] introduced the concept of indentation Schmid factor defined as the ratio of the maximum resolved shear stress to the maximum contact pressure:

$$S = \frac{1}{p_0} \max_{(v),x,y,z} \left| \tau_R^{(v)}(x,y,z) \right| \tag{11}$$

As a usual Schmid factor, the indentation Schmid factor is used in Section 4 to predict the onset of plasticity when $\max_{(v),x,y,z} \left| \tau_R^{(v)}(x,y,z) \right| = \tau_c^{(v)}$ where $\tau_c^{(v)}$ is the critical shear stress corresponding to the pop-in load. However, from Eqs. (10) and (11) a non-uniform stress field is considered to compute S. In Section 4, $\tau_c^{(v)}$ will be found from the experimental values of pop-in loads to be close to the theoretical shear strength for dislocation nucleation.

3.4. Indentation Patel–Cohen factor for martensitic transformation

In the case of the nanoindentation loading of a SMA single crystal, a similar analysis may be performed considering the transformation strain induced by the formation a single variant of martensite denoted (v):

$$\varepsilon_{ij}^{T} = g R'_{ij}(v) \tag{12}$$

where g is the characteristic displacement magnitude of the transformation independent on variant system (v) and $R'_{ij}(v)$ is the orientation tensor. The lattice deformation responsible for phase transformation in SMA requires the interface plane between martensite and the untransformed austenite to be invariant. As the Bain homogeneous lattice deformation does not allow to keep such an invariant plane, this deformation is coupled with a rotation and an invariant lattice deformation. The invariant lattice deformation can be due to slipping, twinning, or stacking fault. In the case of CuAlBe, stacking fault occurs and induces the displacement magnitude g to be a constant value determined from crystallographic analysis and identical for each variant (v). For a particular variant (v), the orientation tensor $R'_{ij}(v)$ is expressed as follows [35,36]:

$$R'_{ij}(v) = \frac{1}{2}(n_i'^{(v)} m_j^{(v)} + n'_j(v) m_i^{(v)}) \tag{13}$$

where $n_i'^{(v)}$ and $m_i^{(v)}$ are respectively the normal to the habit plane and the direction of transformation of the variant (v) (24 variant systems will be considered for CuAlBe crystals like in [2,35]). Unlike the slip direction for crystal plasticity, the direction of transformation is not contained in the habit plane.

As an extension of Patel–Cohen criterion for martensitic transformation initially applied to macroscopic homogeneous loading [35,37], the driving force for martensitic transformation is expressed as a function of the transformation strain, the stress field beneath the indenter for an elastic state and a temperature term related to the chemical energy:

$$F_d^{(v)}(x,y,z) = g R'_{ij}(v)\, \sigma_{ij}(x,y,z) + B(T - T_0) \tag{14}$$

where T is the room temperature, T_0 is the equilibrium temperature at which the volume fraction of austenite equals the volume fraction of martensite, T_0 and B are material constants.

As the term $B(T-T_0)$ is a material constant at fixed room temperature, it may be disregarded in the calculation of the driving force. Thus, for the following discussions on the Patel–Cohen factor, only the first term of Eq. (14) is needed:

$$F_d^{(v)}(x,y,z) = g R'_{ij}(v)\, \sigma_{ij}(x,y,z) \tag{15}$$

The condition for a variant of martensite to appear in austenite (forward transformation) is that the driving force of this variant reaches a critical force F_c [37]:

$$F_d = F_c \tag{16}$$

By analogy to plasticity occurrence by dislocation nucleation [27] a new criterion to determine the activation of martensitic transformation under nanoindentation loading is here introduced as the indentation Patel–Cohen factor S_{PC} defined as

$$S_{PC} = \frac{1}{p_0} \max_{(v),x,y,z} \frac{F_d^{(v)}(x,y,z)}{g} \tag{17}$$

where F_d is computed from the indentation contact stress field (Eq. (5)). Eq. (17) not only gives the indentation Patel–Cohen factor, but also the determination of the first martensite variant to appear beneath the indenter and the location of the activation of this variant.

3.5. Criterion for reverse transformation

Conversely, the indentation Patel–Cohen factor can also be applied to the reverse transformation (from the martensitic structure to the austenitic parent phase) assuming the parent phase is in a purely elastic state beneath the indenter. This criterion describes the last event occurring before a complete return to austenitic state. For a same variant, the expression for the driving force F_d is the same for reverse and forward transformations (Eq. (15)) except that the stress states are different. The condition for the last variant of martensite to transform back in austenite is that the driving force of this variant reaches a critical force equal to $-F_c$ [35]:

$$F_d = -F_c \tag{18}$$

Thus, the load hysteresis ΔF between direct and reverse transformation writes:

$$\Delta F = 2F_c \tag{19}$$

4. Results and discussion

4.1. Dislocation activation in nickel

The Schmid and Boas's convention for slip systems [111] $< 0\bar{1}1 >$ of f.c.c. structures were used for computations on Ni (12 independent slip systems). Using Eqs. (11) and (5), the indentation Schmid factor S has been computed and its dependence on crystallographic orientation is represented on Fig. 1 using an inverse pole figure. The distribution of S forms a set of concentric circles as opposed to the ellipses of the uniaxial loading case as already observed by Li et al. [27]. From Fig. 1 the maximum indentation Schmid factor is found at the center of these circles

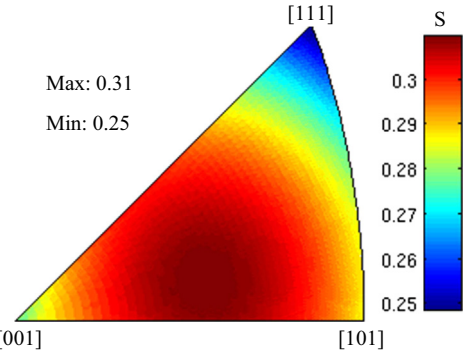

Fig. 1. Inverse pole figure of the indentation Schmid factor S defined from Eq. (11) for Ni single crystal.

i.e. close to a [123] crystal orientation. Conversely, the minimum indentation Schmid factor is close to the [111] crystal orientation.

It is found that the indentation Schmid factors distribution in the inverse pole figure is similar to the one reported in [27]. Only a slight difference is observed with the results of [27] regarding the maximum and minimum values of S (respectively 0.27 and 0.23 in [27]). It is noteworthy that Li et al. [27] performed same calculation under the hypothesis of an elastically anisotropic solid while isotropic elasticity is assumed in the present calculation.

Fig. 2a shows the nanoindentation load-displacement curves on Ni using a Berkovich indenter. The first part of the loading curves can be very well described by the anisotropic Hertzian curves, estimated from the Vlassak and Nix effective moduli [28,29]. For a better understanding of Fig. 2a, the isotropic Hertzian estimate was plotted instead of these anisotropic Hertzian curves, and gives a convenient estimate of the first elastic regime. In Fig. 2a a clear excursion event is observed on each curve at loads of $\sim 114 \pm 11$ μN. Irreversible plasticity activation is evident according to the large residual displacement observed after unloading. Similar load-displacement curves have been reported in the literature for different orientations of Ni [38,39], which means that the experimental procedure used in this study is relevant for the study of excursion events. Fig. 2b focuses on the beginning of the load-displacement curves, anisotropic Hertzian curves are plotted using reduced modulus calculated in Section 3.1 for ideal orientations: $E_r^{111} = 187$ GPa, $E_r^{101} = 184$ GPa and $E_r^{001} = 172$ GPa. A very good fit is found between theoretical anisotropic Hertzian estimate and the first elastic regime for the three grains despite the non ideal orientation of grains A_1, A_2 and A_3. Regarding Eq. (1) it is clear on this figure that: $E_{eff}^{111} > E_{eff}^{101} > E_{eff}^{100}$ which is in agreement with Section 3.1. Furthermore, Fig. 2 shows a dependence of the pop-in load to crystallographic orientation. The load at which the onset of the displacement burst occurs is denoted P_c and ranges as follows: $P_c^{111} > P_c^{100} > P_c^{101}$.

Table 3 presents the average pop-in load for plasticity activation versus the computed indentation Schmid factor for the three studied crystallographic orientations. The pop-in loads in the table correspond to an average made on six nanoindentation tests for grains A_1 and A_2, and on 13 tests for grain A_3. These average pop-in loads are in good agreement with Salehinia et al.'s [40] nanoindentation tests performed on pure Ni with a 100 nm radius tip. This study found the same ranging of the pop-in loads as in [40].

From Eqs. (7) and (11) an estimate of the critical resolved shear stress τ_c under Hertzian contact is given by [27]

$$\tau_c = S\left(\frac{6P_cE_r^2}{\pi^3R^2}\right)^{1/3} \tag{20}$$

We assume that plasticity activation occurs when τ_c equals the theoretical shear strength τ_{th} of the material. From Eq. (20), the calculated estimates of τ_{th} are reported in Table 3. The uncertainties are calculated considering the errors on the effective tip radius (see Section 2.3), the average pop-in load (see Table 3) and the reduced modulus (evaluated to be 2 GPa). Since the shear modulus G of Ni is ~73 GPa [30], τ_{th} is found to be about $G/15$, which is within the classical range of the theoretical shear strength τ_{th}: $G/5$–$G/30$. Using the isotropic assumption (i.e. $S = 0.31$), isotropic elasticity in Eq. (1) and the average pop-in load for the 3 orientations, the obtained value of isotropic τ_{th} is very close to the one reported by Shim et al. [38].

Clearly, as for a usual Schmid factor, the load for plasticity activation is higher in a grain oriented in the [111] direction and presenting a low indentation Schmid factor (~0.26) than in a grain with an orientation close to [101] showing a higher indentation Schmid factor (~0.3). This relation between theory and experiments shows the relevance of the indentation Schmid factor concept.

4.2. Martensitic transformation activation in CuAlBe

Martensitic transformation in CuAlBe is the transformation from a D03 austenite structure to a 18R martensite crystal. Martensite may appear under the form of 24 variants characterized by their habit plane normal n', displacement direction m and displacement magnitude g. These parameters may be calculated by adapting the WLR theory [36] on martensitic transformation to CuAlBe alloys [41]. Values used for $n'^{(v)}_i$, $m'^{(v)}_j$ and g in this study are those proposed by Siredey et al. [35]: $g = 0.22$, $\{a_n, b_n, c_n\}$ {0.168, 0.688, 0.705} and $\{a_m, b_m, c_m\}$ is {0.121, 0.678, 0.725}. From these parameters the transformation strain may be computed for the 24 martensite variants. The driving force for martensitic transformation is calculated, using Eq. (15). The Patel–Cohen factors distribution for uniaxial tests on CuAlBe are represented inside the [001] unit triangle of the inverse pole figures in Fig. 3.

A clear asymmetry of the material behavior is observed between tensile and compressive loading paths. This phenomenon has been explained by Patoor et al. [42] as a loss of symmetry between the austenitic parent phase and the orthorhombic martensitic phase. This low symmetry of the martensitic phase implies transformation strains, so the activation criterion, to depend on the loading path. As a consequence different variants are activated whether the loading is tension or compression. The Patel–Cohen factors range from 0.1 to 0.5 for a tensile test whereas from 0.08 to 0.5 for a compressive loading path.

Fig. 4 shows the distribution of indentation Patel–Cohen factors in an inverse pole figure.

The indentation Patel–Cohen factors distribution displayed in Fig. 4 seems to form a set a concentric arcs of circles with a maximum at the center, close to the [001] direction, as opposed to arcs of ellipses for uniaxial loading (Fig. 3). Resulting indentation Patel–Cohen factors for the three grains B_1, B_2 and B_3 considered experimentally are presented in Table 4.

The S_{PC} values obtained for grains B_1 and B_2 are very close to the maximum indentation Patel–Cohen factor with $S_{PC} \sim 0.31$. Thus it is expected that pop-in load should be higher for grain B_3 which presents an indentation Patel–Cohen factor close to the minimum with $S_{PC} \sim 0.23$.

It has been observed on NiTi SMA that pop-in events due to phase transformation occur at very low forces, under 80 μN [24]. Furthermore studies on CuAlNi, another copper-based SMA, have shown pop-ins due to martensitic transformation occurring at a load level of ~300 μN [43]. This is why the maximum load used for nanoindentation tests performed on CuAlBe was first set to 100 μN. This setting was relevant for [001] oriented grains, where several excursion events were observed. However, as shown in Table 4, pop-in load for the first displacement burst should be higher for grain B_3 than for grains B_1 and B_2. The maximum load had then to be set up

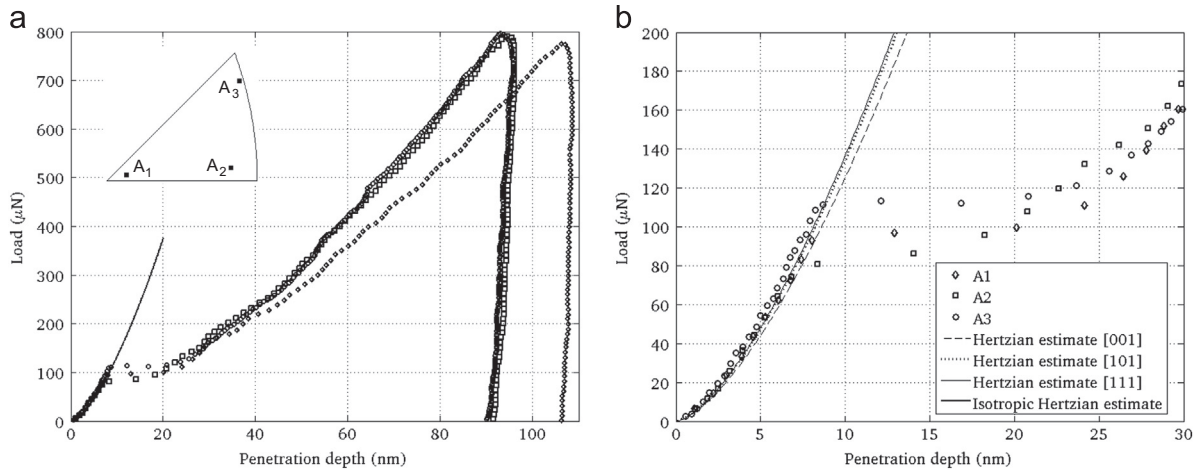

Fig. 2. (a) Representative load-displacement nanoindentation curve for the grains A_1, A_2, A_3 of the Ni specimen with orientations respectively close to [001], [101] and [111] and Hertzian solution with isotropic elasticity, (b) magnified view of the plot shown in (a) exhibiting the first displacement burst and Hertzian solution with anisotropic elasticity.

Table 3
Average measured pop-in load for Ni and estimated indentation Schmid factor from Eq. (11) and theoretical shear strength from Eq. (20) for the [001], [101] and [111] crystallographic orientations and in the isotropic assumption.

Crystal orientation	Average pop-in load (μN)	Indentation Schmid factor	Estimated τ_{th} (GPa)
[101]	103 ± 38	0.30	5.97 ± 1.55
[001]	108 ± 58	0.29	5.43 ± 1.11
[111]	125 ± 50	0.26	5.49 ± 1.17
Isotropic	112 ± 49	0.31	6.12 ± 1.42

to a higher value (500 μN) for tests performed on grain B_3 (with an orientation close to [111]).

Fig. 5 shows nanoindentation tests performed on grains B_1, B_2 and B_3 of the CuAlBe specimen. For grains B_2 and B_3 the initial loading well matches with elastic contact theory, deviating from the Hertzian estimate with a first displacement burst. The Hertzian estimate for grain B_1 does not fit exactly the initial loading, which may be explained by an incomplete unloading of the previous cycle. Several pop-in events follow this first excursion and pop-out events are also observed during the unloading stage. Penetration depth at the end of unloading is almost back to its initial value for grain B_1 (the residual strain is around 0.5 nm) and is equal to zero for grains B_2 and B_3 as the final unloading joins back the initial loading (as a typical tensile test of a superelastic CuAlBe at the macroscopic scale).

AFM images performed on the SMA indented surface after complete unloading showed no evidence of remnant impressions. This comforts the observation that nanoindentation tests on CuAlBe result in almost complete strain recovery. Thus, the observed excursion events on this material are not due to irreversible dislocation plasticity as in Ni. However, due to a first displacement burst, the curve deviates from the elastic regime showing an inelastic mechanism. Presence of excursion events during both loading and unloading and of no residual displacement leads to interpret this inelastic mechanism as reversible phase transformation. These results reveal the spatiotemporal discontinuity of phase transformation propagation at the nano scale.

Displacement bursts on the CuAlBe specimen exhibit a slight slope, whereas in Ni the excursion event is clearly a plateau. This difference in the pop-in (and pop-out) slope is thought to be due to the difference in the observed mechanism between dislocation and martensite variant activation.

For the three grains, the elastic Hertzian curves were calculated from the anisotropic reduced modulus according to Section 3.1, considering the closest ideal orientation: [001] for grains B_1 and B_2 and [111] for grain B_3. Reduced moduli were calculated using Eq. (2) and considering the effective modulus in the ideal orientation: $E_r^{111} = 119$ GPa and $E_r^{001} = 91$ GPa. Resulting anisotropic Hertzian estimates (Eq. (1)) for ideal [001] and [111] orientations are plotted respectively in Fig. 5a and b for [001] and Fig. 5c for [111]. These curves give a very convenient estimate of the first elastic regime of the austenite for the three grains. Fig. 5d shows the anisotropic Hertzian estimates for [001] and [111] ideal orientations. It is concluded that the slope of the anisotropic Hertzian curve for a [111] orientation is higher than for the [001] orientation. As these curves give a convenient fit of the first elastic regime for both orientations, it shows the non-negligible influence of elastic anisotropy on the first elastic regime when the material is in the austenitic state.

Nanoindentation curves presented Fig. 5 show several displacement bursts during both loading and unloading. For grains B_1 and B_2 three excursion events occur after the first displacement burst during loading and the unloading curve shows four displacement bursts. For grain B_3 seven pop-in events are observed during loading and the unloading stage presents seven displacement bursts. Pop-in and pop-out loads are presented in Table 5 for the three grains. It is observed in Table 5 that the pop-out loads for the three grains are close from pop-in loads but slightly lower. It is also observed that at each pop-in during loading corresponds a pop-out during unloading. Thus we can interpret each pop-in as being associated with the activation of martensite variants and the corresponding pop-outs as describing reverse transformation of these variants.

Nanoindentation curves obtained on grains B_1, B_2 and B_3 all start with an elastic loading followed by a first displacement burst. This first pop-in occur at loads of 20 ± 5 μN for grains with an orientation close to [001] and at a load of 55 μN ± 10 μN for grain B_3 with an orientation close to [111]. The load at which the onset of the displacement burst occurs is denoted Pc and ranges as follows: $P_c^{111} > P_c^{100}$. These experimental results are in good agreement with the theoretical indentation Patel–Cohen factors predicting an easier variant activation on the [001] orientation compared to the [111] orientation. These experimental data clearly show a crystallographic orientation dependence of martensitic transformation activation at the nanoscale.

From Eqs. (7), (15) and (17) an estimate of the critical force F_c is deduced:

$$F_c = gS_{PC}\left(\frac{6P_cE_r^2}{\pi^3R^2}\right)^{1/3} \quad (21)$$

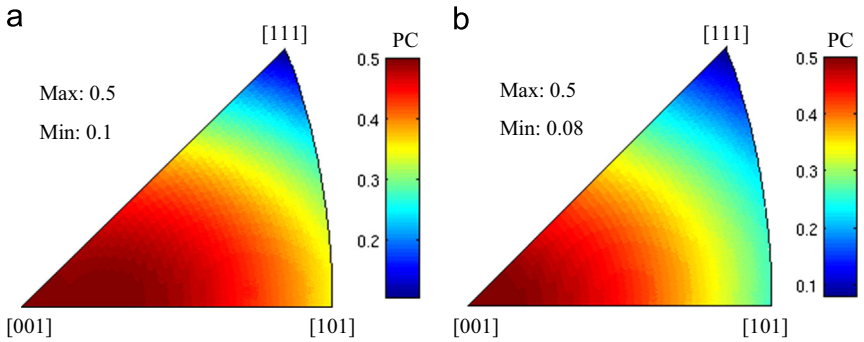

Fig. 3. Inverse pole figure of the Patel–Cohen factors (PC) for a CuAlBe single crystal under (a) tensile (b) compressive loading paths.

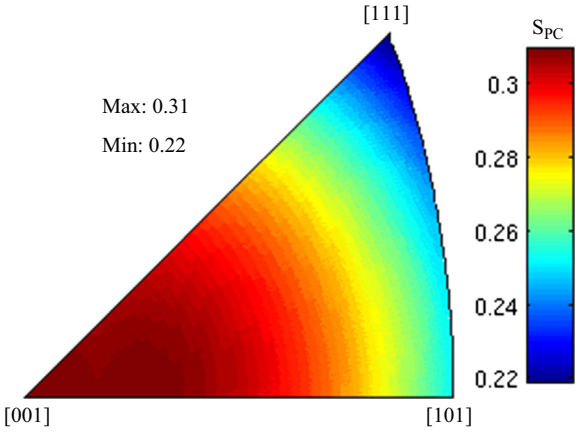

Fig. 4. Inverse pole figure representing the indentation Patel–Cohen factor S_{PC} plotted for CuAlBe single crystal.

Table 4
Indentation Patel–Cohen factor for grains B_1, B_2 and B_3 of the superelastic CuAlBe specimen.

Grain	B_1	B_2	B_3
S_{PC}	0.309	0.310	0.233

Calculated critical forces from Eq. (21) and corresponding load hysteresis (Eq. (19)) are reported in Table 6 for grains B_1, B_2 and B_3. Uncertainties of these values were calculated considering the errors on the effective tip radius (see Section 2.3), the average first pop-in load (see Table 6) and the reduced modulus (estimated to be 2 GPa). The isotropic value of F_c was estimated using the isotropic assumption (i.e. $S_{PC}=0.31$), isotropic elasticity in Eq. (1) and the average pop-in load for the 3 grains. The obtained isotropic value of F_c.is reported in Table 6 and is significantly higher than critical forces estimated under anisotropic hypothesis. This reveals the influence of anisotropy on the calculation of critical forces.

Critical forces were calculated in the case of a bulk polycrystalline CuAlBe specimen under tensile loading path. Internal stress tensors for a [111] and a [001] oriented grains were taken from Kaouache [44] and inserted in Eq. (15). Resulting critical forces for a bulk CuAlBe specimen under tensile loading path were respectively about 62 MPa and 63 MPa. Values of the critical force obtained by nanoindentation are about 240 MPa, which is significantly higher than in bulk material. According to San Juan et al. [43] the density of microstructural defects for preferential martensite activation in bulk materials are grain boundaries, dislocations and stress-concentrated surface defects. However in this study, parameters were set to limit all of these effects because:

(i) nanoindentation experiments were located at the center of the grains to avoid any interaction with grain boundaries,
(ii) specimens were carefully polished and electropolished prior to any nanoindentation experiment in order to avoid surface defect effects,
(iii) the affected studied volume is very small.

Then the density of preferential microstructural points for martensite activation was likely very low, leading to a higher critical force. This explains the significant difference between the critical forces obtained by nanoindentation and the critical forces of a bulk material under tensile test.

5. Conclusion

A theoretical study and nanoindentation experiments at small loads were performed on superelastic CuAlBe SMA to determine the crystallographic orientation dependence of stress-induced martensitic transformation activation revealed by pop-in and pop-out events. The main conclusions are the following:

- The relevance of the nanoindentation procedure for pop-in events detection was first studied. The validation of the stress analysis was performed on the indentation Schmid factors. Experimental and modeling validations were made on Ni with successful comparison with an earlier study [27] regarding the obtained distribution of indentation Schmid factors. The theoretical shear strength of Ni was estimated considering both isotropic and anisotropic assumptions. Good agreement was found between the isotropic calculated value and the literature [38]. A dependence of the theoretical shear stress with crystallographic orientation (and with the indentation Schmid factor) was observed like in [27].
- A new criterion called “indentation Patel–Cohen factor”, and based on continuum thermo-micromechanics associated with Hertzian elastic contact theory is investigated to predict the activation of the first martensite variant beneath the indenter as a function of austenite crystal orientation. It is also shown that this criterion can be applied to the prediction of the last pop-out load corresponding to the reverse phase transformation from martensite back to (elastic) austenite.
- Evidence of discrete stress-induced martensite variants activation is observed on nanoindentation curves of a CuAlBe superelastic SMA according to complete strain recovery and displacement bursts during both loading and unloading. Each pop-in is interpreted as the activation of one martensite variant and the

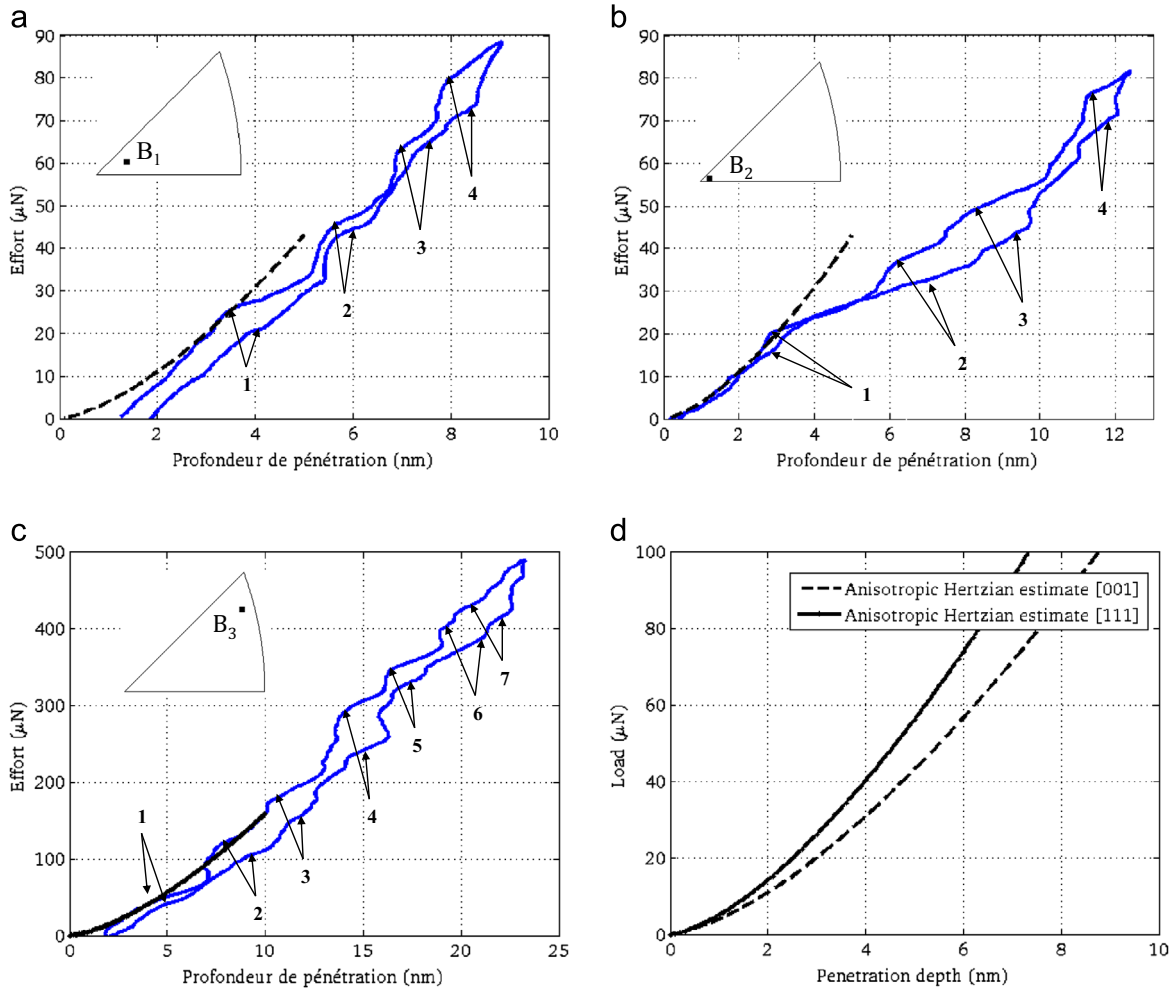

Fig. 5. Resulting load-displacement curves of nanoindentation tests performed on the superelastic CuAlBe specimen on grains (a) B_1, (b) B_2 and (c) B_3 and Hertzian solution with anisotropic elasticity (dashed line). (d) Hertzian solution with anisotropic elasticity for ideal [001] and [111] orientations.

Table 5
Pop-in and pop-out loads (in μN) and hysteresis loads for grains B_1, B_2 (orientation close to [001]) and B_3 (orientation close to [111]) determined for a superelastic CuAlBe SMA.

	Pop-in loads (μN)			Pop-out loads (μN)			Hysteresis loads (μN)		
	B_1 (± 5 μN)	B_2 (± 5 μN)	B_3 (± 10 μN)	B_1 (± 5 μN)	B_2 (± 5 μN)	B_3 (± 10 μN)	B_1 (± 3 μN)	B_2 (± 3 μN)	B_3 (± 10 μN)
1	25	20	55	15	15	25	10	5	20
2	45	35	125	40	30	80	5	5	45
3	65	45	175	65	35	130	5	10	40
4	80	75	290	70	65	235	10	10	55
5	–	–	350	–	–	320	–	–	25
6	–	–	400	–	–	380	–	–	20
7	–	–	420	–	–	390	–	–	30

Table 6
Average measured first pop-in load, estimated indentation Patel–Cohen factor from Eq. (17), estimated critical force from Eq. (21) and load hysteresis for the three CuAlBe indented grains.

Grain	Average first pop-in load (μN)	Indentation Patel–Cohen factor S_{PC} (Eq. (17))	F_c (MPa) (Eq. (21))	ΔF (MPa) (Eq. (19))
B_1	25 ± 5	0.309	233 ± 65	465 ± 130
B_2	20 ± 5	0.310	217 ± 65	433 ± 130
B_3	55 ± 10	0.233	273 ± 63	546 ± 126
Isotropic	33 ± 7	0.31	290 ± 65	580 ± 129

corresponding pop-out as the reverse transformation of this variant, showing the spatiotemporal discontinuity of phase transformation propagation.

- The measured pop-in load for martensitic transformation activation was found to depend on crystal orientation. Tests performed on a [111] oriented CuAlBe grain showed a higher pop-in load than tests led on [001] oriented crystals, showing a good agreement with the theoretical prediction of the indentation Patel–Cohen factor.
- The critical force for stress-induced martensite activation was found to be significantly higher when deduced from

nanoindentation measurements than from tensile tests on a bulk material due to the paucity of microstructural points for preferential martensite activation.

As perspectives of this work, it is envisaged to compute the stress field using full anisotropic elasticity hypothesis for the prediction of the first activated martensite variant beneath the indenter. Furthermore, finite element analyses will be performed to study the influence of the stress field due to the first variant on the subsequent activation of other variants.

Acknowlegments

The authors are grateful to Région Lorraine under "CPER 2007–2013" and to the French Agence Nationale de la Recherche (ANR) under contract "PHIRCILE" (ANR 2010 JCJC 0914 01) for financial support of the Nanoindenter. The calculations were performed with the scientific computing code Simula+ developed in the French laboratories LEM3 (Metz), CEMES (Toulouse) and LAMAV (Valenciennes).

Appendix

Stress components at some arbitrary position (x, y, z) due to a concentrated normal point force p_0 acting on the surface of an elastic half-space (Johnson [33]):

$$\tilde{\sigma}_{xx} = \frac{1}{2\pi}\left[\frac{(1-2\nu_s)}{r^2}\left\{\left(1-\frac{z}{\rho}\right)\frac{x^2-y^2}{r^2}+\frac{zy^2}{\rho^3}\right\}-\frac{3zx^2}{\rho^5}\right] \quad (A.1-1)$$

$$\tilde{\sigma}_{yy} = \frac{1}{2\pi}\left[\frac{(1-2\nu_s)}{r^2}\left\{\left(1-\frac{z}{\rho}\right)\frac{y^2-x^2}{r^2}+\frac{zx^2}{\rho^3}\right\}-\frac{3zy^2}{\rho^5}\right] \quad (A.1-2)$$

$$\tilde{\sigma}_{zz} = -\frac{3\,z^3}{2\pi\rho^5} \quad (A.1-3)$$

$$\tilde{\sigma}_{xy} = \frac{1}{2\pi}\left[\frac{(1-2\nu_s)}{r^2}\left\{\left(1-\frac{z}{\rho}\right)\frac{xy}{r^2}-\frac{xyz}{\rho^3}\right\}-\frac{3xyz}{\rho^5}\right] \quad (A.1-4)$$

$$\tilde{\sigma}_{xz} = -\frac{3\,xz^2}{2\pi\,\rho^5} \quad (A.1-5)$$

$$\tilde{\sigma}_{yz} = -\frac{3\,yz^2}{2\pi\,\rho^5} \quad (A.1-6)$$

where ν_s is the isotropic Poisson ratio, $\rho = \sqrt{x^2+y^2+z^2}$ and $r = \sqrt{x^2+y^2}$.

References

[1] E. Patoor, D.C. Lagoudas, P.B. Entchev, L.C. Brinson, X. Gao, Mech. Mater. 38 (2006) 391–429.
[2] C. Niclaeys, T. Ben Zineb, E. Patoor, J. Phys. IV 112 (2003) 175–178.
[3] Y. Chemisky, A. Duval, E. Patoor, T. Ben Zineb, Mech. Mater. 43 (2011) 361–376.
[4] W.C. Oliver, G.M. Pharr, J. Mater. Res. 7 (1992) 1564–1583.
[5] A. Kuntz, S. Pathak, J.R. Greer, Acta Mater. 59 (2011) 4416–4424.
[6] W.W. Gerberich, J.C. Nelson, E.T. Lilleodden, P. Anderson, J.T. Wyrobek, Acta Mater. 44 (1996) 3585–3598.
[7] A. Gouldstone, H.-J. Koh, K.-Y. Zeng, A.E. Giannakopoulos, S. Suresh, Acta Mater. 48 (2000) 2277–2295.
[8] D.J. Morris, S.B. Myers, R.F. Cook, J. Mater. Res. 19 (2004) 165–175.
[9] D.F. Bahr, D.E. Kramer, W.W. Gerberich, Acta Mater. 46 (1998) 3605–3617.
[10] C.A. Schuh, A.C. Lund, J. Mater. Res. 19 (2004) 2152–2158.
[11] M.J. Cordill, N.R. Moody, W.W. Gerberich, Int. J. Plast. 25 (2009) 281–301.
[12] Y.L. Chiu, A.H.W. Ngan, Acta Mater. 50 (2002) 1599–1611.
[13] S. Vadalakonda, R. Banerjee, A. Puthcode, R. Mirshams, Mater. Sci. Eng. A 426 (2006) 208–213.
[14] J. Pfetzing-Micklich, R. Ghisleni, T. Simon, C. Somsen, J. Michler, G. Eggeler, Mater. Sci. Eng. A 538 (2012) 265–271.
[15] T.-H. Ahn, C.-S. Oh, D.H. Kim, K.H. Oh, H. Bei, E.P. George, H.N. Han, Scr. Mater. 63 (2010) 540–543.
[16] J. Woirgard, C. Tromas, J.C. Girard, V. Audurier, J. Eur. Ceram. Soc. 18 (1998) 2297–2306.
[17] S. Moyne, C. Poilane, K. Kitamura, S. Miyazaki, P. Delobelle, C. Lexcellent, Mater. Sci. Eng. A 273 (1999) 727–732.
[18] A.J. Muir Wood, T.W. Clyne, Acta Mater. 54 (2006) 5607–5615.
[19] M. Arciniegas, Y. Gaillard, J. Peña, J.M. Manero, F.J. Gil, Intermetall 17 (2009) 784–791.
[20] Y. Zhang, Y.-T. Cheng, D.S. Grummon, J. Appl. Phys. 101 (2007) 053507.
[21] W.C. Crone, H. Brock, A. Creuziger, Exp. Mech. 47 (2007) 133–142.
[22] H.-S. Zhang, K. Komvopoulos, J. Mater. Sci. 41 (2006) 5021–5024.
[23] C.P. Frick, T.W. Lang, K. Spark, K. Gall, Acta Mater. 54 (2006) 2223–2234.
[24] X.-G Ma, K. Komvopoulos, J. Mater. Res. 20 (2005) 1808–1814.
[25] B. Kaouache, S. Berveiller, K. Inal, A. Eberhardt, E. Patoor, Mater. Sci. Eng. A (2006) 773–778438–440 (2006) 773–778.
[26] J. Pfetzing-Micklich, C. Somsen, A. Dlouhy, C. Begau, A. Hartmaier, M.F.-X. Wagner, G. Eggeler, Acta Mater. 61 (2013) 602–616.
[27] T.L. Li, Y.F. Gao, H. Bei, E.P. George, J. Mech. Phys. Solids 59 (2011) 1147–1162.
[28] J.J. Vlassak, W.D. Nix, Phil. Mag. A 67 (1993) 1045–1056.
[29] J.J. Vlassak, W.D. Nix, J. Mech. Phys. Solids 42 (1994) 1223–1245.
[30] G. Simmons, H. Wang, Single Crystal Elastic Constants and Calculated Aggregate Properties: A Handbook, second ed., MIT, Cambridge, 1971.
[31] F.M. Sánchez-Arévalo, G. Pulos, Mater. Charact. 59 (2008) 1572–1579.
[32] D. Rios-Jara, A. Planes, Ll. Mañosa, J. Ortin, S. Belkahla, M. Morin, G. Guénin, J. L. Macqueron, J. Phys. IV 1 (1991) 283–288.
[33] K.L. Johnson, Contact Mechanics, first ed., Cambridge University Press, Cambridge, 1985.
[34] W.H. Press, S.A. Teukolsky, W.T. Vetterling, B.P. Flannery, Numerical Recipes, third ed., Cambridge University Press, New-York, 2007.
[35] N. Siredey, E. Patoor, M. Berveiller, A. Eberhardt, Int. J. Sol. Struct. 36 (1999) 4289–4315.
[36] M.S. Wechsler, D.S. Lieberman, T.A. Read, Trans. AIME 197 (1953) 1503–1516.
[37] J.R. Patel, M. Cohen, Acta Metall. 1 (1953) 531–538.
[38] S. Shim, H. Bei, E.P. George, G.M. Pharr, Scr. Mater. 59 (2008) 1095–1098.
[39] S.K. Lawrence, D.F. Bahr, H.M. Zbib, J. Mater. Res. 27 (2012) 3058–3066.
[40] I. Salehinia, S.K. Lawrence, D.F. Bahr, Acta Mater. 61 (2013) 1421–1431.
[41] J. De Vos, E. Aernoudt, L. Delaey, Z. Metallkd. 69 (1978) 438–455.
[42] E. Patoor, M. El Amrani, A. Eberhardt, M. Berveiller, J. Phys. IV 5 (1995) 495–500.
[43] J. San Juan, M.L. Nó, C.A. Schuh, Acta Mater. 60 (2012) 4093–4106.
[44] B. Kaouache, Analyse multiéchelles de la transformation martensitique induite par contrainte dans les alliages à mémoire de forme. Corrélation contraintes-microstructure, Ecole Nationale d'Arts et Métiers, 2006. (Ph.D. dissertation).